RESEARCH ARTICLE | MARCH 08 2024

Terahertz radar with all-dielectric leaky-wave antenna

Harrison Lees **≅** ⊚ ; Daniel Headland ⊚ ; Shuichi Murakami; Masayuki Fujita ⊚ ; Withawat Withayachumnankul ⊚



APL Photonics 9, 036107 (2024)

https://doi.org/10.1063/5.0180941

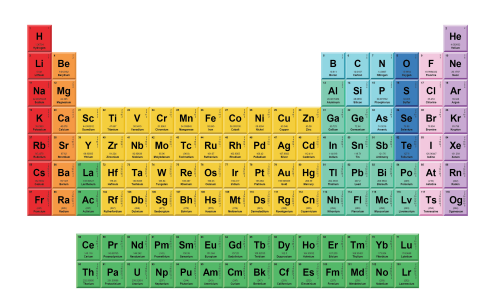
A CHORUS















Terahertz radar with all-dielectric leaky-wave antenna

Cite as: APL Photon. 9, 036107 (2024); doi: 10.1063/5.0180941 Submitted: 13 October 2023 • Accepted: 5 February 2024 • Published Online: 8 March 2024







Harrison Lees,^{1,a)} Daniel Headland,² Shuichi Murakami,³ Masayuki Fujita,⁴ and Withawat Withawachumnankul¹

AFFILIATIONS

- ¹ Terahertz Engineering Laboratory, The University of Adelaide, Adelaide, SA 5005, Australia
- ²Optoelectronics and Laser Technology Group, Department of Electronics Technology, Universidad Carlos III de Madrid, 28911 Leganés, Spain
- Osaka Research Institute of Industrial Science and Technology, 2-7-1 Ayumino, Izumi, 594-1157 Osaka, Japan
- ⁴Graduate School of Engineering Science, Osaka University, Toyonaka 560-8531, Japan

ABSTRACT

Terahertz radars based on leaky-wave antennas are promising for the realization of radar systems with high resolution over short ranges. This type of radar relies on spatial frequency mapping to realize a wide field of view without mechanical actuation or electrical beam steering. Previously, integrated leaky-wave antennas based on metallic wave confinement have been implemented, but the high ohmic losses limit the realized antenna gain, which is essential for extending the range of such a system when limited power is available. Here, we demonstrate an all-dielectric leaky-wave antenna fabricated monolithically from silicon and then apply leaky-wave radar techniques to realize a terahertz radar system capable of real-time data acquisition. Through this all-dielectric approach, we can avoid metallic losses, achieving an experimentally measured maximum realized gain of 25 dBi and a 34.3° 3-dB field-of-view while utilizing established and scalable fabrication techniques essential for the wide-spread adoption of terahertz technologies. We foresee this technique being applied to a variety of real-time radar applications, and here we demonstrate two potential use-cases: multi-object tracking and differentiation of liquids.

© 2024 Author(s). All article content, except where otherwise noted, is licensed under a Creative Commons Attribution (CC BY) license (http://creativecommons.org/licenses/by/4.0/). https://doi.org/10.1063/5.0180941

I. INTRODUCTION

The use of terahertz frequencies for radar applications offers unique opportunities in terms of resolution and object penetration. In particular, the shorter wavelength compared to traditional microwave radar enables resolutions on the order of millimeters as opposed to meters. In addition, terahertz waves have the ability to penetrate non-metallic, dry materials, many of which are typically opaque to light detection and ranging (LIDAR). The combination of these properties defines a niche where terahertz waves are uniquely suited for the detection of small targets that are optically hidden from the viewer.

The earliest terahertz radars were based upon terahertz time domain spectroscopy, ^{2,3} using optically pumped photo-conductive antennas in combination with a mechanical delay line to realize ultra-broadband systems with depth resolutions on the order

of micrometers. However, there exist several fundamental barriers to the practical application of these systems. First, they rely on mechanical actuation to realize in-plane beam scanning, which, when combined with long integration times results in impractically long acquisition times, for real-time tracking. Second, these systems are typically bulky and far from portable, while only producing nano-watts of terahertz power, which is rapidly dispersed due to path loss, limiting the effective range. The combination of these factors makes the prospect of wide spread adoption of such a system for ranging and localization improbable.

In competition with terahertz time domain spectroscopy, terahertz frequency modulated continuous wave radars have emerged, 4-6 capable of improved range due to higher output powers at the expense of bandwidth and, hence, depth resolution. To realize beam steering, a quasi-optical reflector is typically mechanically actuated with a piezo-electric or otherwise mechanical stage.

a) Author to whom correspondence should be addressed: harrison.lees@adelaide.edu.au

This mechanism is much faster than raster-scanning but still results in an inherent trade-off between achieved resolution and measurement times, while the chirp time required and the impact of phase noise become increasingly important.⁷

These points were addressed through the use of leaky-wave antennas (LWA) in combination with a frequency swept terahertz transceiver as a terahertz radar. Solution 10 Without mechanical parts, the size and complexity of the system are significantly reduced, while the innate frequency scanning of leaky-wave antennas enables single shot imaging of a single plane with a wide field of view—a critical capability in the terahertz regime where broadband, efficient, and integrated phase-shifters for the realization of phased arrays are still elusive. Hence, for applications where reduced resolution is permissible, particularly for localization, the practical advantages of an integrated system are significant.

Previously, terahertz leaky-wave antennas have been proposed for a variety of platforms, including all silicon, 11,12 silicon on an insulator, 13 3D-printed cyclic olefin copolymer (COC), 14 3D-printed alumina, 15 hollow metallic waveguides, 9 terahertz microstrip lines, 16 parallel plate waveguides, ^{17,18} spoof surface polariton waveguides, ¹⁹ and indium-phosphide.²⁰⁻²² Many of these antennas utilize metals for mode confinement, hindering the maximum realized gain due to ohmic losses incurred. Those that do not include metals are narrow bands due to frequency dependent coupling mechanisms 11-13 or reliance on photonic bandgap crystals.¹⁵ Alternatively, waveguides realized monolithically from high-resistivity float-zone silicon could be utilized to instantiate a leaky-wave antenna. In recent years, substrateless silicon waveguides^{23–25} have been used to realize a range of passive components, 26,27 including a variety of high gain end-fire antennas.^{28–30} This approach is attractive as the intrinsic material losses of these devices are nearly negligible, ensuring very high radiation efficiency. As long as coupling to free space is managed carefully, conserving the limited terahertz power can be generated with currently available sources. More recently, terahertz sources and detectors have been integrated to form simple terahertz systems on a chip, 31,32 enabling the possibility of future fully integrated radar systems based on all-silicon waveguides. In this context, we aim to consolidate the practical advantages of frequency scanning antennas for radar applications with a high efficiency dielectric waveguide platform, focusing on the development of a high gain frequency scanning antenna.

The proposed antenna utilizes continuous fast-wave leakage between a dielectric waveguide and an adjacent dielectric slab, ^{33–36} negating the need for scattering elements typical of a periodic LWA. This is critical for a substrateless, dielectric, leaky-wave antenna where the lack of a metallic ground plane for shielding makes it difficult to suppress the undesired symmetry that arises from the radiating elements, which results in a halving of the power radiated in the desired direction. In infrared photonics, this can be partially addressed through the use of apodized grating structures, ³⁵ although to realize this asymmetry, a multi-stage etching process would need to be employed, increasing the fabrication complexity.

It is noted that the design of this antenna was previously expounded in our numerical study,³⁴ and here we expound thereupon with more-detailed information about the design, experimental validation, and a demonstration of terahertz-range radar.

The following paper is divided into four sections. First, we design an all-silicon leaky-wave antenna with an auxiliary dielectric lens. Then, we perform a thorough experimental characterization of this antenna to determine its suitability and limitations for radar applications. Finally, we derive a single shot imaging algorithm for de-embedding the depth and angular information from complex-valued reflection measurements, including an analysis of the limit of the achievable depth and angle product. We provide two illustratory demonstrations for applications of terahertz radar: first, multi-object tracking, and second, in-container liquid differentiation.

II. ANTENNA DESIGN

Previously, an integrated frequency division multiplexer was proposed based upon in-slab beam-forming of slab modes launched by fast-wave leakage from an unclad dielectric waveguide into an adjacent dielectric slab.33 In this case, the leakage rate and radiation angle are controlled by the separation between the waveguide core and the slab. As the guided waves propagate in the dielectric waveguide, they undergo phase change with respect to distance in addition to gradually leaking power. This translates to a wide aperture distribution with a linearly ramped phase. In the cited work, in-slab focusing at a desired point is achieved by compensating for this change in phase by progressively shortening the distance from the slab edge to that point, resulting in convex curvature. Thus, the leaked terahertz waves that enter the slab via these convex-curved boundaries will constructively interfere at the aforementioned point, forming a focus. Critically, due to the dispersion of both the waveguide and slab modes, the location of this focus is frequency-dependent, resulting in a frequency-scanning focus that may be collected at different points in the slab, thereby achieving frequency-division multiplexing. By placing the focus in the farfield, a collimated frequency-scanning beam is launched rather than a focused beam, and this is the basis of the antenna that is the main subject of the present work.

The antenna is composed of three connected stages, as depicted in Fig. 1. The leakage channel is a dielectric waveguide, which guides the fundamental E_x^{11} mode as it is continuously leaked into an adjacent dielectric slab. This slab is bordered by a gradient-index (GRIN) anti-reflection coating realized by etched holes in the silicon slab; this facilitates the conversion of the slab mode into free-space. Then an external astigmatic lens is used for H-plane collimation, designed to enhance the far-field gain of the antenna package. The following sub-sections describe the design of each component individually.

A. Uniform leakage wave tunneling

A slow-wave waveguide will not leak energy into free space without radiating elements to introduce a discontinuity, as is commonly utilized in scatterer based, periodic leaky-wave antennas.³⁷ In lieu of scattering elements, an intermediary medium is required to induce power leakage, and in this case, a dielectric slab serves this purpose. This slab is capable of supporting its own guided slab mode with a slower wave speed than the waveguide mode, which induces a gradual power transfer from the waveguide mode into the slab mode by a process of evanescent coupling, also known as wave-tunnelling.

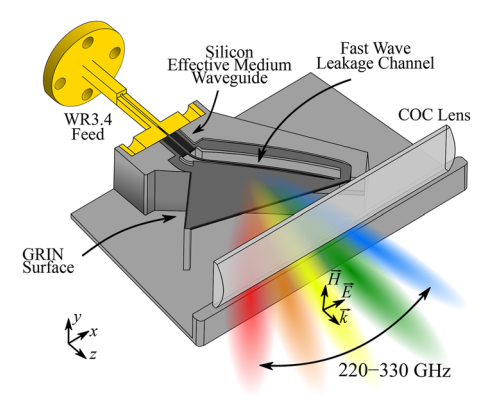


FIG. 1. Proposed leaky-wave radar module. A schematic drawing of the proposed leaky wave radar package highlights the various components, including the fast-wave leakage channel, the GRIN anti-reflection coating, and the auxiliary cyclicolefin-copolymer (COC) lens. These elements are mounted in a fixture, 3D printed from polylactic acid (PLA), and designed such that they do not interfere with the device's operation.

It is intuitive that as the separation between the waveguide and the slab is reduced, the degree of overlap of the evanescent fields will increase, accelerating the rate of leakage and increasing the modal index of the waveguide, which is now loaded by the nearby slab. Previously, a theoretical analysis of the leakage between a dielectric waveguide and an adjacent slab was presented to quantify these relations, which was later verified by full-wave simulation. In Figs. 2(a)–(c), the critical outcomes of this analysis for the E_x^{11} waveguide mode are presented for a high-resistivity float-zone waveguide core of width 200 μ m and an adjacent slab, both with a thickness of 250 μ m, with separations varying from 20 to 200 μ m. Here, we adopt a realistic permittivity of 11.68 and neglect material losses as the loss tangent, $\tan \delta$, is known to be less than 1.5×10^{-5} at these frequencies. 39

The leakage profile is indicative of the effective aperture of the antenna—a larger aperture corresponds to a higher gain. In this case, a uniform leakage profile is desired, with an aperture of 14.5 mm. This design process is performed at the center frequency, 275 GHz, and as such, the performance degrades as the operating frequency deviates from this point. In Fig. 2(a), at low frequencies, the rate of leakage accelerates rapidly, causing rapid leakage and, thus, a poor aperture is formed. At high frequencies, the rate of leakage is limited, leading to residual power in the guide even with long trailing channels at the minimum fabricable separation of 20 μ m, limiting the efficacy of the antenna at these frequencies.

In Fig. 2(b), we observe the dispersive nature of this leakage mechanism, and from the phase constants of the slab and the wave-guide loaded by the nearby slab, the leakage angle as shown in Fig. 2(c) is derived as

$$\sin \theta_{\text{Leakage}} = \frac{\beta_{\text{Waveguide}}}{\beta_{\text{Slab}}}.$$
 (1)

The combination of these factors limits the maximum achievable bandwidth of this scheme.

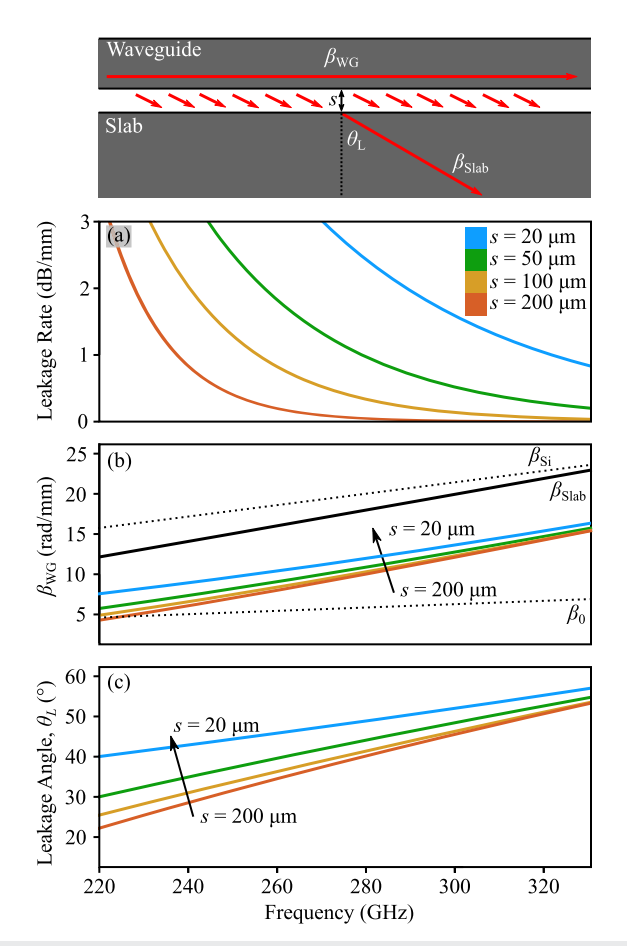


FIG. 2. Characteristics of waveguide-slab leakage. (a) Leakage rate from guided to slab mode for various waveguide-slab separations. (b) Phase constant of waveguide mode when loaded by slab at various separations. (c) Launch angle of the slab mode arising from leakage from the waveguide.

Using the relationship between separation, leakage rate, and leakage angle, an iterative design algorithm described previously³³ can be implemented to determine the necessary separation and waveguide curvature required to project a beam into the far-field. The separation between the waveguide and the slab is designed in three sections in order to achieve the leakage profile shown in Fig. 3(a). First, the waveguide is gradually introduced to the slab to avoid a sudden index discontinuity while allowing low frequency components to leak. Then the separation is tailored to induce a uniform leakage profile; to achieve this, the separation is gradually decreased until the minimum possible separation is reached. Finally, a long trailing section with the minimum viable separation is introduced; this is critical to improve performance at higher frequencies where slow leakage results in residual power in the waveguide after the uniform leakage region. The separation between the waveguide and adjacent slab across the length of the channel is shown in Fig. 3(b). The beam formation is achieved by a lateral offset of the waveguide relative to the feed, as shown in Fig. 3(c). This offset compensates for the accumulated phase as

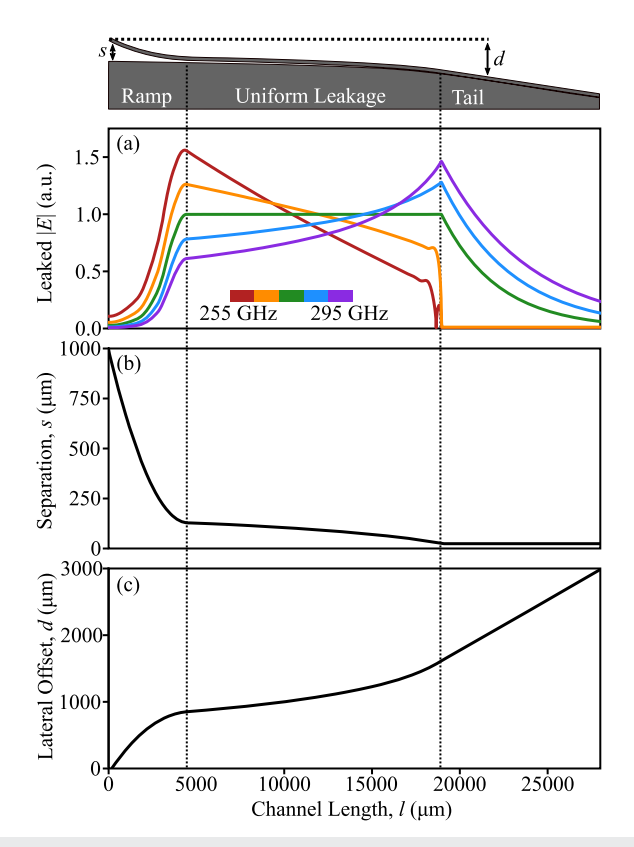


FIG. 3. Design of the continuously leaking waveguide. (a) Desired leakage profile for the formation of a uniform aperture at 275 GHz. The separation between the waveguide and the slab (b) and the lateral offset (c) are designed such that the leakage profile in (a) is achieved while the desired focus is in the far-field.

the wave propagates along the feed waveguide, ensuring that the phase profile of the leaked wave is ramped, generating a collimated beam at the output, which is essential for realizing high far-field gain.

B. GRIN anti-reflection structure

In this antenna, the dielectric slab acts as an intermediary medium for broadband, scatterer-free leakage but ultimately acts as an obstacle to the effective transfer of terahertz power from the waveguide to free space. The Fresnel losses at the edge of the slab increase with the incident angle, until ultimately total internal reflection occurs at, the critical angle $\theta_c \approx 18^{\circ}$, calculated as $\theta_c = \arcsin(n_0/n_{\rm Si})$. To overcome this, the boundary of the slab is angled such that the center frequency is normally incident, ensuring that across the operating band the incident angle remains below the critical angle and Fresnel losses are minimized. However, these losses are still not negligible, even at small incident angles. Compounding this, the component of the beam that is reflected at this interface will continue to propagate internally until it is eventually radiated, forming undesirable side lobes, or is dissipated at the input as additional reflection loss. For these reasons, an anti-reflection scheme is essential.

In optics, a related problem arises in the design of solar cells. In order to couple light into high-index dielectrics as the sun passes through the sky, varying the incident angle, GRIN optics are utilized to overcome weak transmission at oblique incident angles. ^{40–42} In particular, quintic index transitions have been shown to be a simple, compact, and effective mechanism to realize efficient matching over a broad range of incident angles. In this case, a gradient index can

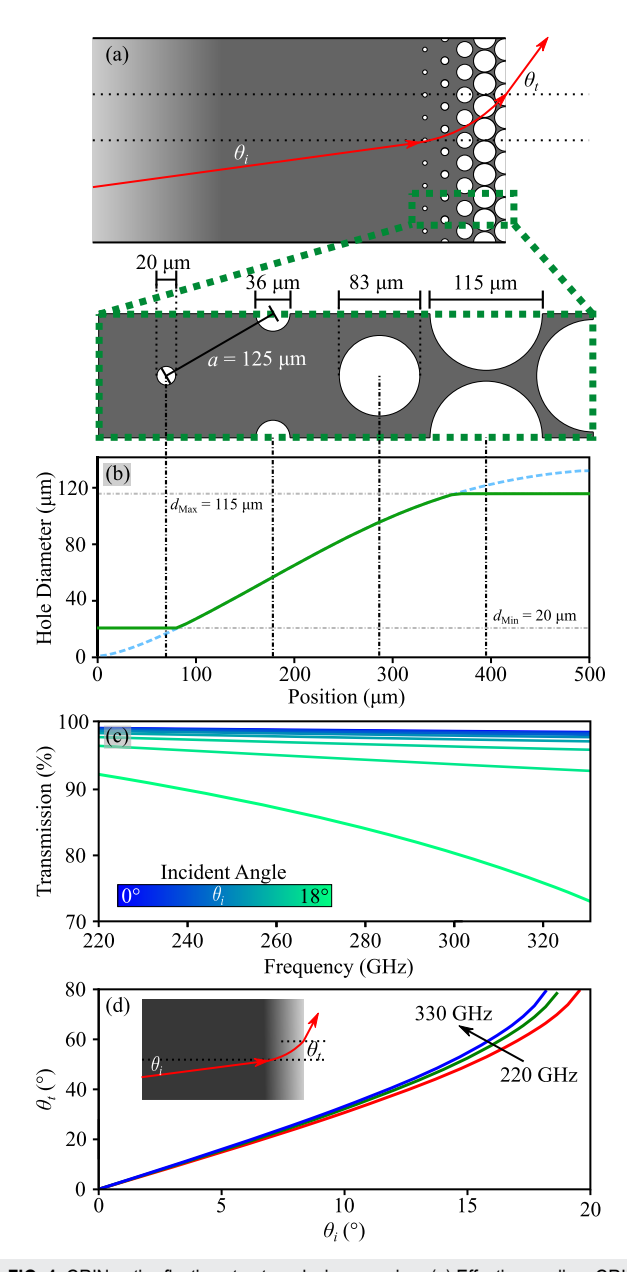


FIG. 4. GRIN anti-reflection structure design overview. (a) Effective medium GRIN anti-reflection coating used to match the slab mode into free space. (b) Quintic gradient curve used to design this anti-reflection structure, showing the cropping due to fabrication constraints. (c) Broadband transmission of the GRIN structure derived through the discretized ray tracing method.

be realized through the perforation of the silicon slab with cylindrical holes arranged in a hexagonal lattice, as long as the lattice period has a deep sub-wavelength period; hence, the lattice period, a = 125μm is selected. The Maxwell–Garnet approximations,⁴³ in combination with the transcendental solution for the slab mode index,⁴⁴ can be used to derive the range of achievable indices. Then, using these values, the quintic gradient index distribution can be calculated.⁴¹ Due to fabrication constraints, the minimum possible hole diameter is 20 µm, and in order to maintain the mechanical stability of the structure, the maximum diameter is limited to 115 μ m. At 275 GHz, these correspond to modal indices of 3.00 and 1.28, respectively, incurring some residual discontinuity between the slab mode, the GRIN structure, and free space. In Fig. 4(a), this matching scheme is outlined with a single unit cell of the GRIN anti-reflection coating highlighted, with hole diameters corresponding to the gradient in Fig. 4(b).

To validate the performance of this design, a ray-tracing model is implemented to simulate the transmission of slab mode through the gradient index structure at various incident angles. The GRIN structure is discretized into 30 segments, modeling the transition from silicon into free-space via the GRIN structure, with each segment's refractive index corresponding to the modal index of a silicon slab perforated uniformly with holes of diameter shown in Fig. 4(b). Then Snell's Law and Fresnel coefficients are applied iteratively at each interface to calculate the final transmission magnitude and transmitted angle. This process is repeated at each frequency to account for the slab mode dispersion, yielding the results shown in Figs. 4(c) and 4(d), respectively. Here, transmission efficiency is in excess of 95% for incident angles up to 17°, corresponding to a maximum transmitted angle after refraction of 70°, incidentally expanding the field-of-view of the antenna.

C. 3D printed COC lens

The out-of-plane radiation pattern of this is fundamentally limited by the small physical aperture created by the thin edge of the silicon wafer. This results in a so-called fan-beam, typical of other antennas, which use the slab's edge as a radiating aperture.² many applications, this is undesirable for two reasons: first, it limits the maximum achievable gain of the antenna, and second, the out of plane power can easily result in spurious reflections from the environment, leading to multipath interference. To compensate for this, we propose expanding the transverse aperture with free space optics to form a module with a two-dimensional radiating aperture.⁴⁵ In this case, we design a cylindrical plano-convex lens with a bespoke ray-tracing algorithm and manufacture this lens from a 3D printed cyclic-olefin-copolymer (COC). This lens is designed to correct the fan-beam effect in the out-of-plane dimension while maintaining the frequency scanning beams in the plane, and so a cylindrical lens is a natural choice to correct this astigmatism. In this design process, we assume COC is a lossless, dispersion-less material with a permittivity $\varepsilon_{COC} = 2.31$, in line with previous experimental characterizations. 48 Although the focal length of this lens is a free-variable, for our target application, we desire a compact module, so we select a desired lens cross section of 12 mm and a focal length of 15 mm. Then, 2D ray-tracing is applied to optimize the lens profile y by varying a in the expression $y = ar^2 + d$. The Nelder–Mead method is used

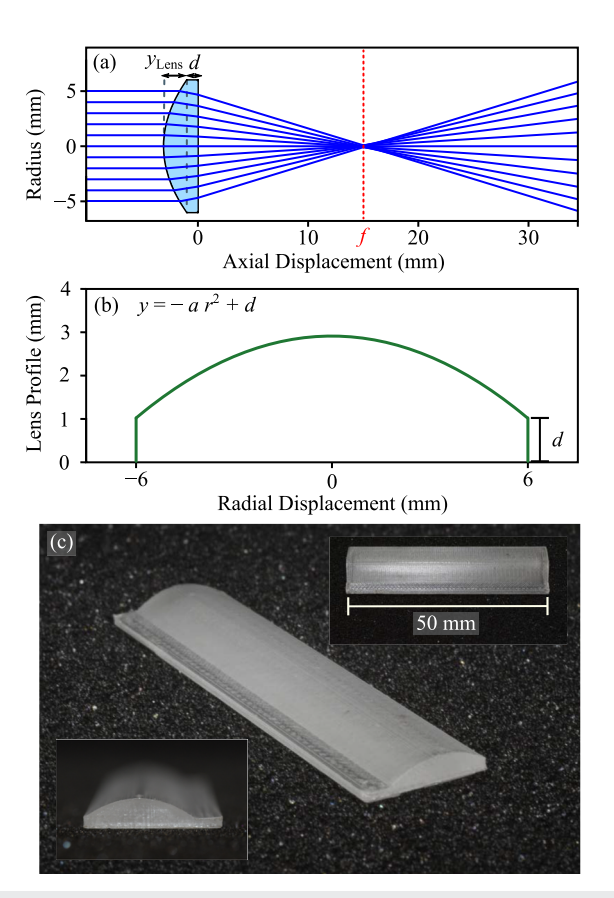


FIG. 5. Auxiliary 3D-printed COC lens. (a) Output from optimization of the parabolic surface via a ray tracing algorithm, with a focus at 15 mm. (b) Optimized lens profile comprising a quadratic surface and a fixed offset, d=1 mm, where a=0.0583. (c) Photograph of a cylindrical lens 3D printed from COC.

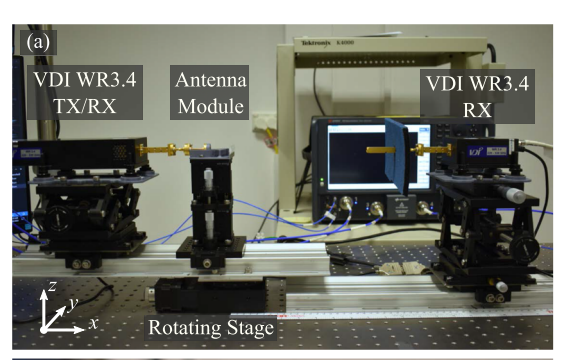
to minimize an objective function, which considers weighted factors arising from the ray-tracing algorithm: the distance between the mean of all ray intersections and the desired focus, and the thickness of the lens.

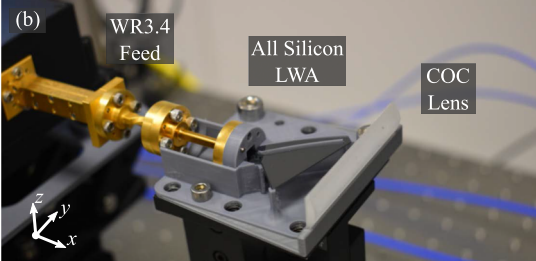
In Fig. 5(a), we present the outcome of this optimization process. As the desired lens is cylindrical, the optimized lens profile is simply extruded to form a 3D solid. The in-plane resolution of this process is limited by the width of the 0.4 mm extrusion nozzle, while the printing layer height is set to 50 μ m. In Fig. 5(c), the surface and internal finish of the lens are imperfect, resulting in a cloudy appearance. It has been shown that this has a small impact on lens performance, as this cloudiness arises from the presence of air in the printed material, which diminishes the aggregate refractive index. 49,50

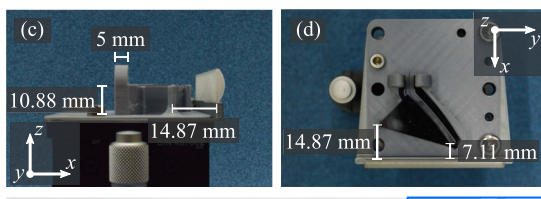
III. ANTENNA CHARACTERIZATION

A. Measurement setup

To validate this design, the device is fabricated from a 250 μm float-zone, high-resistivity silicon wafer with a single mask and a deep reactive ion etch process. Experiments are performed with a







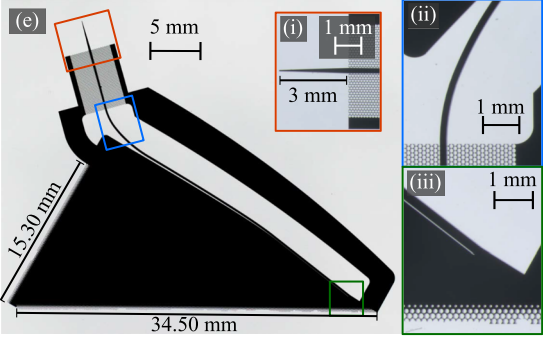


FIG. 6. Experimental setup for antenna characterization. (a) Overview of the experimental setup, showing VDI extension modules aligned with antenna modules on top of a motorized rotating stage for automated radiation pattern measurements. (b) 3D printed antenna module with packaged antenna, integrated COC lens, and rectangular waveguide alignment flange. For practical reasons, we design and package the antenna inside of the 3D printed polylactic acid (PLA), such that the alignment to the feed waveguide and external lens are fixed in place. The mount is designed such that the PLA does not interfere with the electromagnetic wave guide. (c) Side view of the radar module, highlighting key parameters. (d) Top view of the radar module, highlighting the distance from the antenna to the lens. Note that the radiation center of the antenna exists within the slab, such that the edge of the slab is not at the focal length of the lens. (e) Macroscopic image of the fabricated sample with micrographic inserts: (i) feeding taper to be inserted into a rectangular waveguide for efficient coupling, (ii) unclad waveguide section, and (iii) fine resolution features including the leakage channel and anti-reflection structure—with some damage visible arising from incidental overetching during

Keysight N5222B vector network analyzer (VNA) with WR3.4 VDI extension modules. The largest dimension of the physical aperture of the antenna is 35 mm without the lens and 51 mm with the lens, implying Fraunhofer distances of 1.1 and 4.8 m, respectively, and due to practical limitations, we cannot measure the radiation pattern in the far-field. Instead, we measure the radiation pattern in the radiative near-field at a distance of 200 mm. As shown in Fig. 6(a), the antenna module is placed atop a rotating stage such that the phase center of the antenna is centered above the rotating axis. Figure 6(b) shows the fabricated silicon device supported by the 3D printed fixture and coupled to the metallic waveguide feed and COC lens. A computer is used to synchronize the VNA and rotating stage to automatically measure the radiation pattern as the antenna is rotated. In Fig. 6(c), the fabricated device is shown with insert micrographs highlighting the key features of the antenna. To measure the realized gain, we measure S_{21} across the frequency range at each transmission angle with the silicon antenna as the transmitter and another diagonal horn antenna with a known gain in the range of 22-25 dBi across the measured range as the receiver. This measurement is compared to the same measurement performed with a diagonal horn antenna in place of the leaky-wave antenna. The realized gain is calculated as follows:

$$G(f,\theta) = |S_{21,LWA}(f,\theta)| - |S_{21,Horn}(f,0)| + G_{Horn}(f,0) - 20 \log_{10} \frac{d_{LWA}}{d_{Horn}}$$
 (dB), (2)

where $S_{21,\mathrm{LWA}}(f,\theta)$ is the measured transmission with the proposed antenna as a transmitter at a distance of d_{LWA} from the receiver, while $S_{21,\mathrm{Horn}}(f,0)$ is the measured transmission with a horn antenna with gain, $G_{\mathrm{Horn}}(f,0)$, at a distance of d_{Horn} . These measured results are compared to results extracted from full-wave simulation in the commercially available CST Studio Suite 2023, but only in the case without the lens, as the lens' large electromagnetic size makes full-wave simulation impractical.

B. Measured results

In Fig. 7(a), we present the measured reflection, which is below -10 dB across the measured band, highlighting good coupling between the feed and the silicon antenna with reflections in line with the simulated results. Notably, we do not see a significant increase in reflection due to the inclusion of the external lens. Figure 7(b) is the realized gain map of the antenna, showing the frequency sweeping characteristic of leaky-wave antennas, with select frequencies plotted in polar coordinates in Fig. 7(c). Then, Fig. 7(d) contains the maximum gain at each frequency with and without the inclusion of the COC lens. With the COC lens, we observe an average increase in gain of 6.5 dB, suggesting that this lens is effective at collimating the H-plane component as intended. In Fig. 7(e), the approximately linear frequency scanning behavior is described. The maximum gain of 25 dBi is on-par with that of a standard horn antenna.

Here, we note the fabricated sample shows a minor deviation from the simulations, namely, a 3-dB bandwidth of 53.5 GHz as compared to 61.7 GHz in the simulation, while the field-of-view is then compressed to 34.3° compared to 40.0° in the simulation. We attribute these effects to fabrication tolerances, notably inci-

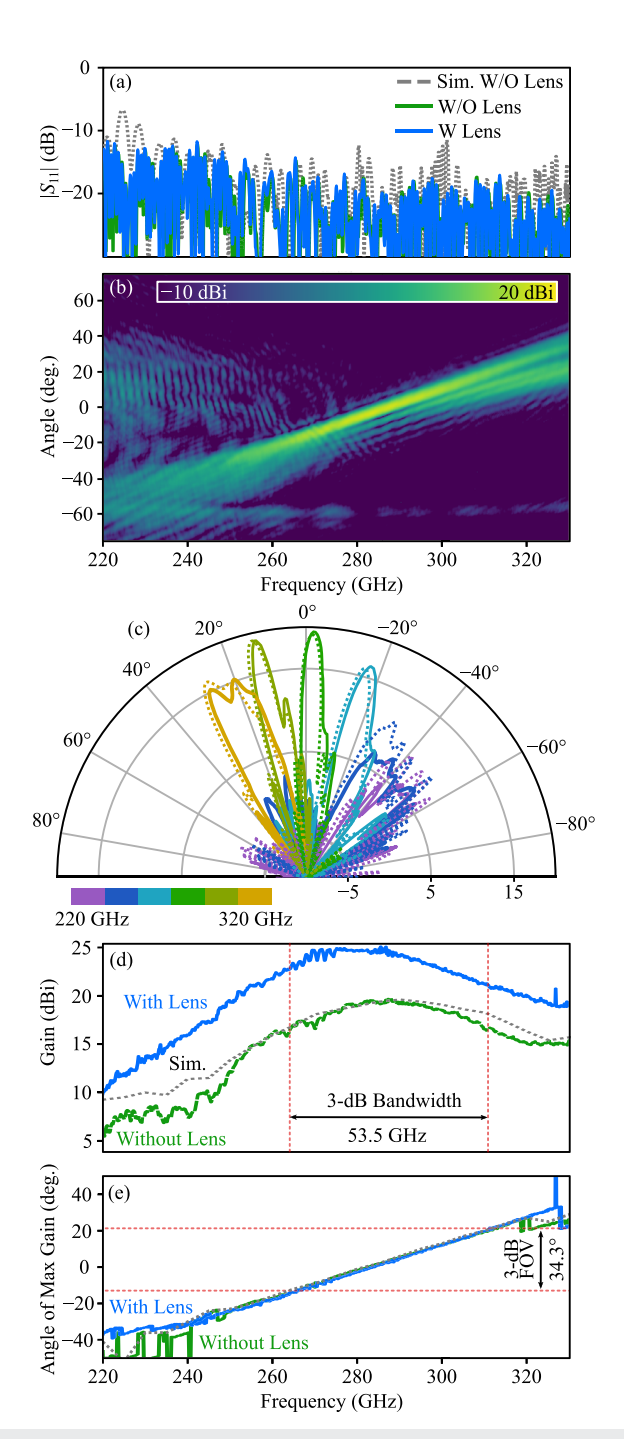


FIG. 7. Experimental characterization of the proposed antenna. (a) Measured reflection coefficients to demonstrate efficient coupling to free space over the measured frequency range. (b) Radiation pattern measurement without lens over frequency and angle of interest showing frequency scanning behavior. (c) Radiation pattern measurements at selected frequencies across the operating band. (d) Maximum gain over frequency, with and without the external COC lens. (e) Angle of the maximum gain over frequency, describing the angular frequency scanning behavior. At either end of the operating band, the relationship between angle and frequency breaks down, resulting in the sudden discontinuities observed in this plot, as a similar gain is observed across a wide range of angles.

dental overetching leading to a narrower than designed waveguide and overside holes in the GRIN structure. As a result, this changes the dispersion relation at the core of the design methodology. A thinner waveguide drives faster leakage from the waveguide as the phase constant of the waveguide diminishes while the relative dispersion between the slab and waveguide is also changed—hence these changes to the leakage profile and scanning angle outside of the design frequency. As visible in Fig. 6(e-iii), overetching also results in some damage to the anti-reflection structure, which may hinder the matching at oblique angles, further suppressing the realized gain. However, generally, the measured simulations confirm the antenna's ability to generate a high gain beam with quasi-linear frequency scanning. In Table I, we compare this antenna's performance to other experimentally demonstrated leaky-wave antennas in the literature.

IV. LEAKY WAVE RADAR

A. Signal processing

With the antenna characterized, we proceed to outline how it can be deployed for single shot angle of arrival imaging based on leaky-wave techniques. Fundamentally, leaky-wave radar is underpinned by the correlation between the received reflections and the mapping between frequency and beam angle. In previous studies, 51,52 the received frequency domain spectra were discretized with fixed windows in order to derive the spatial mapping. Importantly, this approach highlights the fundamental trade-off between depth and angular resolution, with narrower frequency domain windows resulting in higher angular resolution at the expense of range resolution, which is derived from the bandwidth of the window. Previously, the angle of the target is mapped by calculating the frequency at which the maximum change in reflection occurs. In both cases, the range is determined by the inverse-Fourier-transform. We propose that the directivity of the antenna can be used to window the received reflection in the frequency domain in order to achieve angular resolution limited by the beam angle and depth resolution limited by the dispersion of the antenna. In this way, the spatial mapping can be expressed as

$$A(\theta, d) = \mathcal{F}^{-1}(D^2(\theta, f) \cdot S_{11}). \tag{3}$$

In Fig. 8(a), an example S_{11} measurement is shown; this value is multiplied by the radiation pattern shown in Fig. 7(b), and the inverse Fourier transform is applied to form the range map for each angle, with two angles shown in Fig. 8(b), which, when applied to all angles, results in the 2D mapping in polar coordinates as shown in Fig. 8(c).

Based on this approach, we can estimate the angular and depth resolutions based on the antenna's radiation pattern. In Fig. 9(b), the depth resolution is calculated from the 3-dB bandwidth, BW, at each angle with the equation as per the depth resolution of an optical coherence tomography (OCT) system, 53

$$\Delta z = \frac{2 \ln 2}{\pi} \frac{c}{\text{BW} \left(1 - \frac{\text{BW}^2}{4f_c^2}\right)}.$$
 (4)

TABLE I. Comparison of experimentally demonstrated leaky-wave antennas and this work.

Waveguide platform	Max gain (dBi)	3-dB fractional bandwidth (%)	Center frequency (GHz)	3-dB field of view (deg)	Integrated	External lens
Hollow metallic ⁹			415	51	Yes	No
Silicon photonic crystal ¹¹		2	325		Yes	No
Silicon slab ¹²		2	320		Yes	No
Silicon rib ¹³		1	194		Yes	No
COC rib ¹⁴			120		Yes	No
Alumina photonic crystal ¹⁵		10	105		Yes	No
Microstrip line ¹⁶	18	32	275	38	Yes	No
Parallel plate ¹⁸			225	35	No	No
Spoof plasmon polariton ¹⁹	16	41	182.5	30	Yes	No
Substrate integrated ²⁰	15.4	15	60	18.2	Yes	No
Indium phosphide ²¹	11	16	275	40	Yes	No
Indium phosphide ²²	23	16	275	33	Yes	Yes
This work	25	19	275	34.3	Yes	Yes

In addition, when the fractional bandwidth available at each angle is limited, this can be further simplified to

$$\Delta z = \frac{2 \ln 2}{\pi} \frac{c}{BW}.$$
 (5)

In order to achieve the finest possible angular resolution, the frequencies propagated in each direction must be unique so that they can be distinguished from all other angles. In other words, frequency provides a one-to-one mapping to angle. Conversely, to achieve the best possible depth resolution, the entire available bandwidth should be directed uniformly across the field of view, as a broad bandwidth is required to distinguish between subtle differences in time delay. This is a fundamental limitation of leaky-wave radar. We attempt to quantify this trade-off by analyzing the cross-correlation between received signals to retrieve an intuitive definition of the angular resolution of the system. In Fig. 9(a), we show the similarity matrix of the radiation pattern measured previously, defined as

$$\rho_{\theta_i \theta_j} = \frac{\sum_{f_k} G(f_k, \theta_i) \cdot G(f_k, \theta_j)}{\sqrt{\sum_{f_k} G(f_k, \theta_i)^2} \sqrt{\sum_{f_k} G(f_k, \theta_j)^2}},$$
(6)

where a strong correlation between signals when $i \neq j$ implies poor distinguishability and, hence, poor angular resolution. From this, we define the angular resolution as the range of angles for which the correlation between the center angle and adjacent angles exceeds 0.5, as highlighted in Fig. 9(a). In Fig. 9(b), we compare the depth and angular resolution and observe their inverse relationship, postulating that the product of the depth and angular resolution, as shown in Fig. 9(c), should be approximately constant, approaching a theoretical limit in the operating region of the antenna.

To quantify the interrelation between depth and angle resolution, first consider the frequency scanning behavior as a linear relationship between the angle of transmission θ and the central frequency, f_c , such that

$$f_c = (\theta - \theta_{f_{\text{Min}}}) \frac{df_c}{d\theta} + f_{\text{Min}}, \tag{7}$$

where $\frac{df_c}{d\theta}$ is the rate at which the central frequency changes with respect to angle. In actuality, this relationship is implicit in Eq. (1) for small angles, although, as observed in Fig. 2, the relationship over this frequency range is approximately linear. Then, we approximate the radiation pattern of the antenna such that at each angle it is a unity amplitude Gaussian in the frequency domain with a width w_0 such that the FWHM is equal to the channel bandwidth BW, then

$$D(\theta, f) = \exp\left(-\frac{1}{2} \frac{(f - f_c)^2}{w_0^2(\theta)}\right),\tag{8}$$

where

$$w_0 = \frac{BW}{2\sqrt{2 \ln 2}}. (9)$$

Then, assuming a constant beamwidth with respect to the center frequency, the directivity at one angle can be expressed as the directivity at any other angle, with the center frequency shifted such that

$$D(\theta_i, f) = D(\theta_i, f + \Delta f_c). \tag{10}$$

Then, the similarity between the radiation pattern at any two angles, θ_i and θ_j , is contained within the auto-correlation function of $D(\theta_i, f)$, denoted as $D(f) \star D(f)$ (Δf_c), which can be calculated as

$$D(f) \star D(f)(\Delta f_c) = \int D(f)D(f + \Delta f_c)df, \qquad (11)$$

where Δf_c then comes to represent the difference in center frequency between any two angles. Continuing by expanding Eq. (11),

$$D(f) * D(f)(\Delta f_c) = \int \exp\left(-\frac{1}{2} \frac{f^2}{w_0^2}\right) \exp\left(-\frac{1}{2} \frac{(f + \Delta f_c)^2}{w_0^2}\right) df,$$

= $\exp\left(-\frac{1}{2} \frac{(f + \Delta f_c)^2}{(\sqrt{2}w_0)^2}\right).$ (12)



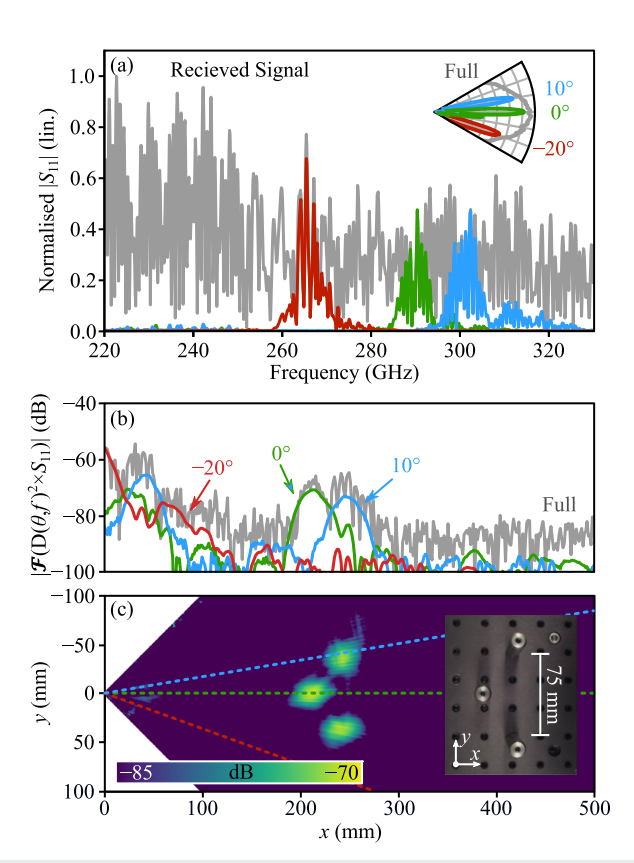


FIG. 8. Visual description of the spatial mapping process used for single shot radar image retrieval. (a) Magnitude of the received signal windowed by the directivity measured at each angle to map the components of the received signal to direction. (b) Inverse Fourier transform is then applied to each complex-valued, windowed component of the received signal to estimate the time domain signal arriving from each angle. In this case, one component shows an empty spectrum (red), while the other component shows a peak at 225 mm (green) and 250 mm (blue). (c) 2D map in Cartesian coordinates, built from this process applied to all angles and then converted from polar to Cartesian coordinates. Here, we can see the recovered radar image and corresponding ground truth, three optical posts arranged in a triangle.

From here, the full width at half maximum, which we have defined as the boundary for similarity, can be easily extracted from the autocorrelation as it is similarly, a Gaussian function,

$$FWHM(f_c) = \sqrt{2} BW. (13)$$

This can be interpreted as the distance from the central frequency required to reduce the auto-correlation to less than 0.5. Hence, by inverting Eq. (7), this expression can be linked to the angular resolution, whereby the received signals at each angle are sufficiently distinguishable from adjacent angles. Rewriting this in terms of scanning angle yields an equation linking the bandwidth to the angular resolution $\Delta\theta$,

$$\Delta\theta = \frac{d\theta}{df_c} \sqrt{2} \text{ BW}. \tag{14}$$

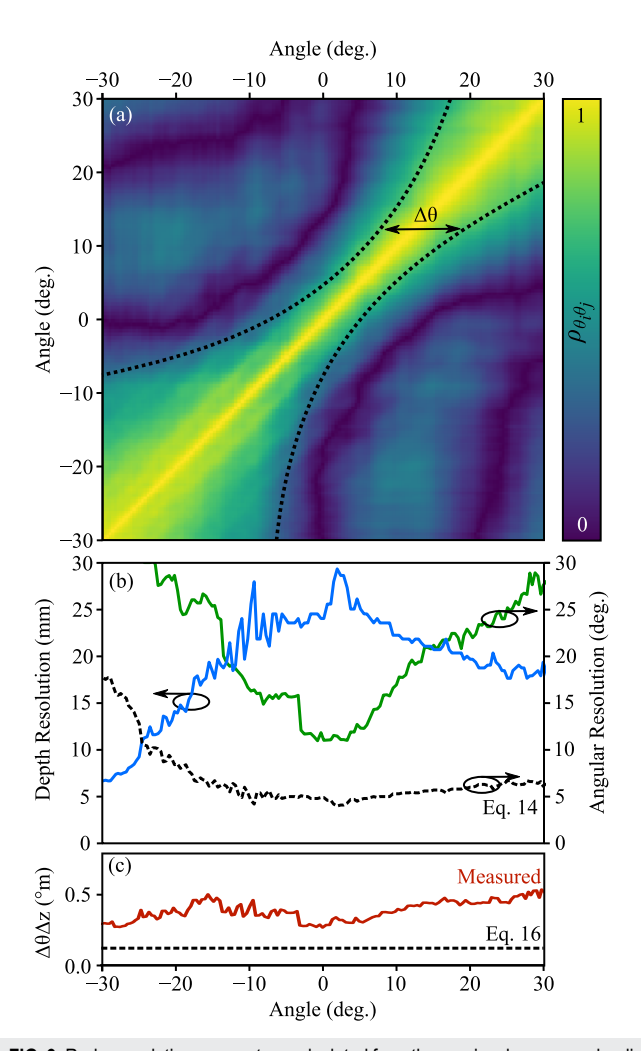


FIG. 9. Radar resolution parameters calculated from the previously measured radiation patterns. (a) Correlation between the gain measured at each angle and the gain measured at every other angle, describing the angular resolution of the system. In this case, a strong correlation with other angles indicates poor angular resolution, as the signal at a given angle is poorly distinguished from other angles. (b) Depth resolution as defined in Eq. (5), and angular resolution as the range of angles for which the similarity between the central angle and the surrounding angles is greater than 0.5. (c) Product of the depth and angular resolution.

Finally, as the depth and angular resolution can both be derived from the bandwidth and central frequency, it is natural to combine them. By combining Eqs. (5) and (14), when the channel bandwidth is sufficiently small, the product of the depth and angular resolutions becomes

$$\Delta z \Delta \theta = \frac{2\sqrt{2} \ln 2}{\pi} \frac{d\theta}{df_c} c, \tag{15}$$

or if we consider this condition in terms of device bandwidth and field of view,

$$\Delta z \Delta \theta = \frac{2\sqrt{2} \ln 2}{\pi} \frac{\text{FOV}_{\text{LWA}}}{\text{BW}_{\text{LWA}}} c. \tag{16}$$

This intuitive result implies that, in order to achieve the best possible resolution product, the ratio of bandwidth to field-of-view should be maximized, and the only way to expand the field-of-view without degrading the resolution is to simultaneously increase the operating bandwidth.

Here, we arrive at a consistent but stricter limitation for the depth-angle uncertainty than previously presented, ⁵⁴ as we apply a more-stringent depth resolution criterion and consider the differentiability of each angular component from the broadband signal. We note that the presented condition is still the best achievable value under ideal leaky-wave frequency scanning, as variable bandwidth, non-linear frequency scanning, non-Gaussian gain profiles, and the presence of sidelobes all degrade the performance. In Figs. 9(b) and 9(c), we observe the impact of these effects by comparing the theoretical values derived here to measured values. We postulate that the presence of side lobes in the antenna radiation pattern is the primary

cause of this difference, as these effects are not accounted for under ideal conditions.

B. Application demonstrations

In this section, we provide a demonstration of two potential applications, multi-object tracking and in-container liquid differentiation, of terahertz leaky-wave radar. For these demonstrations, the vector network analyzer is connected to a computer in order to manage data-acquisition while simultaneously providing real-time radar imaging at $\sim \! 10$ fps. The vector network analyzer sweeps 1001 frequency samples in the operating frequency range of 220–330 GHz, then the computer performs the windowing and inverse-Fourier-transform described in Sec. IV A before generating a plot in polar coordinates. We note that, while a vector network analyzer is used in this case, it is foreseeable that an additional directional coupler to

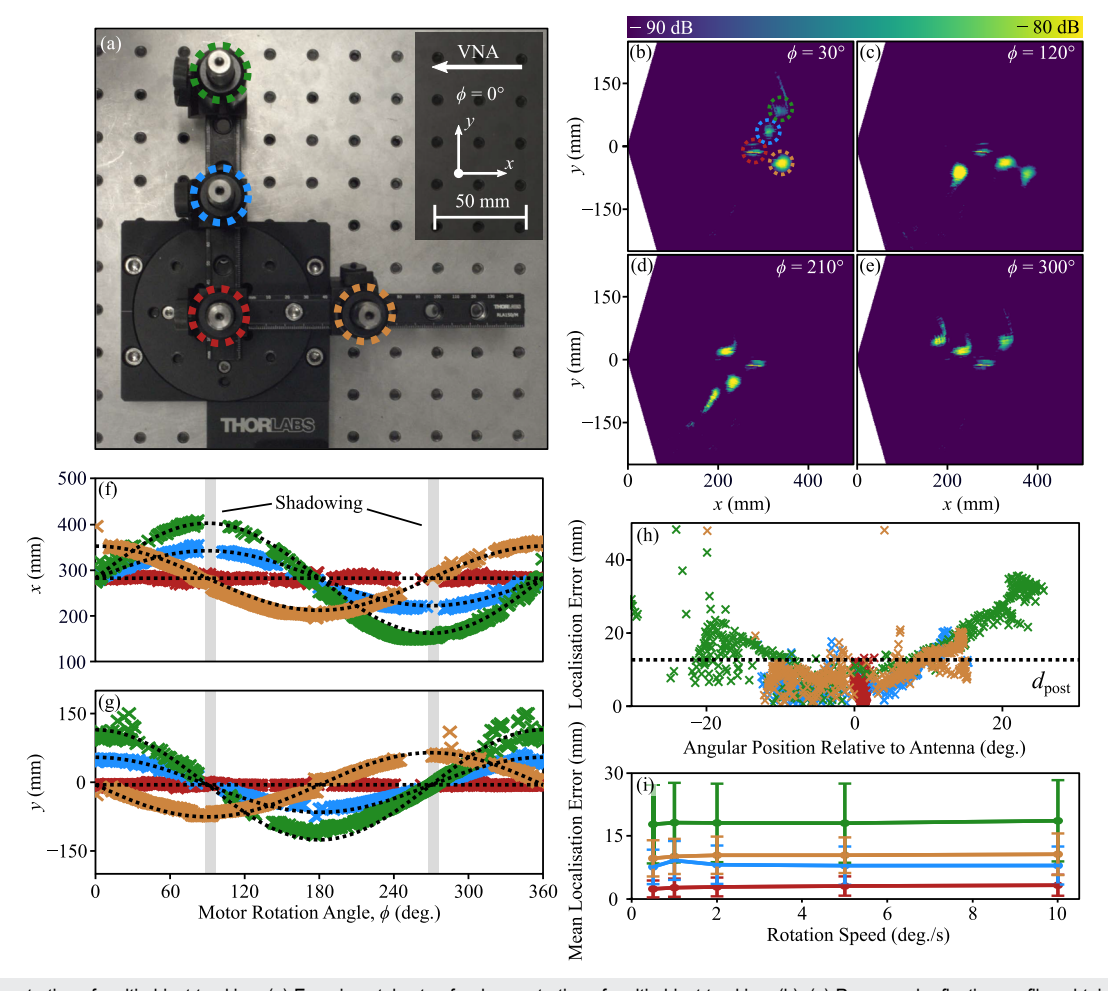
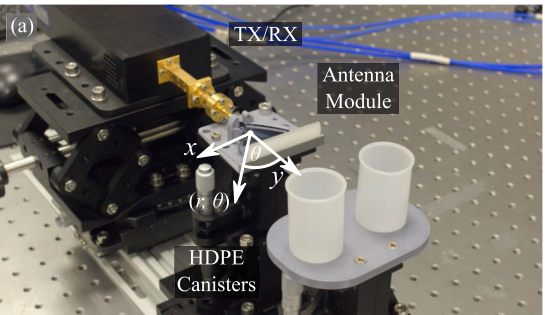


FIG. 10. Demonstration of multi-object tracking. (a) Experimental setup for demonstration of multi-object tracking. (b)–(e) Recovered reflection profiles obtained in real time as the posts are rotated around a common axis, where ϕ is the rotation stage angle. (f)–(g) x and y coordinates of each post, recovered from the radar data using a 2D peak finding algorithm. Black dashed lines represent the actual position of the posts, determined by their known radius and angle. Discontinuities in the measured data occur when a post is shadowed by another post. (h) Error between the recovered and actual positions. We note that this dependency on the angle is consistent with the angular resolution determined in Fig. 9(b). (i) Position error with increasing motor speeds, noting that for the measured speeds, the error is unchanged.

Previously, we described the antenna in terms of 3-dB bandwidth and 3-dB field of view, as these are common standards, although, in practice, the usable bandwidth and field of view are much broader than these common metrics would suggest. Effective spatial mapping is feasible across the linear frequency scanning range, albeit with a much weaker received signal. Hence, the practical field of view is dependent on the dynamic range of the detector—in reality, with our laboratory based system, a field of view of 60°, utilizing frequencies in the range of 240–320 GHz, is effective, and for the following demonstrations, we will utilize the entire spectrum to recover images, which maximizes the retrieved information.

1. Multi-object tracking

The most elementary application of a terahertz radar module is for the detection and range of objects. In contrast to microwave radar, the shorter wavelength enables the detection of small objects while maintaining the ability to penetrate some common obstructions, such as plasterboard or thin screens, which may block monitoring with LIDAR or an ordinary camera. Due to the previously outlined limitations, this technique is not suitable for multi-layer imaging of fine structures typically associated with terahertz technologies. Here, we outline a simple demonstration centered around tracking multiple moving targets simultaneously. As shown in Fig. 10(a), four metallic optical posts with a diameter of 12 mm are placed on a rotating stage at varying radii from the rotation center. Then measurements are made continuously through a full 360° range of motion, with speeds ranging from 0.5° to 10° per second. This demonstrates its suitability for real time tracking. In Figs. 10(b)-10(e), a selection of the single shot frames captured throughout the rotation shows that throughout the scan, multiple objects at various depths and angles can be clearly resolved simultaneously. To quantify the localization accuracy, a 2D peak finding algorithm is applied to each frame to find the position of each post, and the positions determined are shown in Figs. 10(f) and 10(g). In Fig. 10(h), this information is used to calculate the localization error of each post. The error is dependent on the angular position of the post, with higher errors at the edge of the field of view, in line with the angular resolution calculated in Fig. 9(b). Within the 3-dB field-of-view, the localization error is below the diameter of the post, but beyond this range, the localization accuracy is degraded due to the effect of image smearing as the linear relationship between angle and frequency breaks down. Finally, the mean and standard deviation of the error are calculated at various motor speeds, up to the limit of our rotation stage, showing only a small increase in error at these low velocities. To accompany this demonstration, we supply a video showing real-time tracking of an optically obscured object in the supplementary material, 1. In this video, an optical post is hidden behind a sheet of paper. In this case, both the obstruction and the optical post can be localized. We note that the apparent size of the objects is related to the angular and depth resolution of the system and the angle of reflection. This results in similar apparent sizes for the metallic post and the paper.



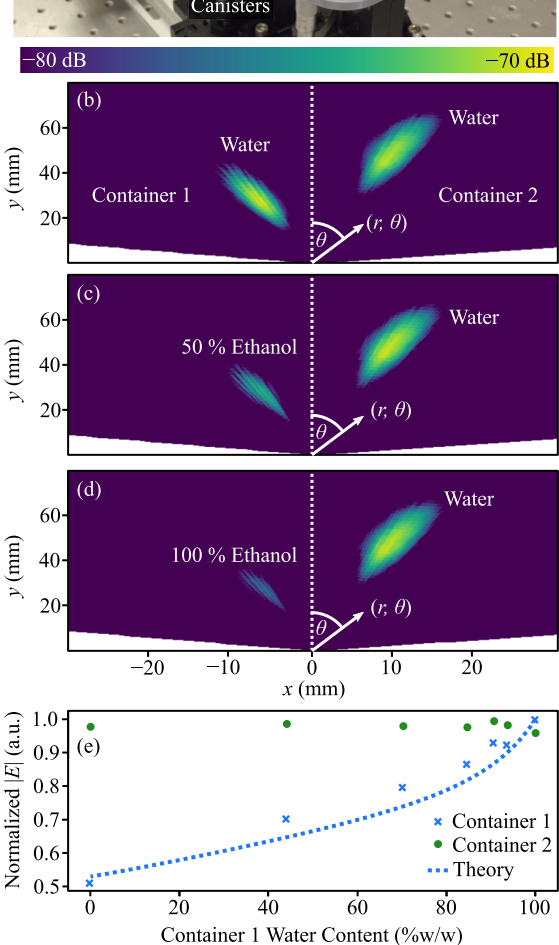


FIG. 11. Demonstration of liquid differentiation. (a) Experimental setup for demonstration of the ability to differentiate between container liquids. (b) Reflection profile of two HDPE containers, both containing water. (c) Reflection profile when one container contains a 50% v/v ethanol solution and the other contains water. (d) Reflection profile when one container contains ethanol and the other contains water. (e) The peak amplitudes of each container as the water/ethanol proportion of container 1 is varied.

2. In-container liquid differentiation

A second potential application is in a front-line test for the differentiation of liquids that appear identical under visual inspection or are obscured by an opaque container. In contrast to common chemical analysis, this technique is non-destructive, and as the radiation is non-ionizing, this technique can be applied without the need for shielding. Reflectometry is a common technique for quickly differentiating liquids based on the contrast in their reflection or transmission characteristics. Here, we apply this technique qualitatively to mixtures of two common liquids: $^{56-58}$ ethanol, $n_{\rm Ethanol} = 1.70 - 0.21j$, and water, $n_{\rm Water} = 2.52 - 1.11j$, contained within High Density Polyethylene (HDPE) film canisters, 59 $n_{\rm HDPE} = 1.53$. Without the depth resolution to distinguish the reflection from the air-HDPE interface from the HDPE-liquid interface, we must consider the measured amplitude as the sum of the two individual reflections from each surface. In line with previous work on this topic, $^{56-58,60}$ we model the normalized reflection magnitude as

$$\frac{E_R}{E_0} = |\rho_{0,\text{HDPE}}| + |\tau_{0,\text{HDPE}}\tau_{\text{HDPE},0}\rho_{\text{HDPE},\text{Sample}}|, \tag{17}$$

where the first term represents the reflection from the air-HDPE interface at the outer surface of the container, and the second term represents the reflection from the inside surface of the container. The Fresnel coefficients $\rho_{i,j}$ and $\tau_{i,j}$ are the Fresnel reflection and transmission coefficients, respectively, calculated as

$$\rho_{i,j} = \frac{\hat{n}_i - \hat{n}_j}{\hat{n}_i + \hat{n}_j}, \qquad \tau_{i,j} = \frac{2\hat{n}_i}{\hat{n}_i + \hat{n}_j}, \tag{18}$$

We assume that the loss from transmission through the thin HDPE is negligible and ignore the curvature of the container. We model the aqueous ethanol solutions with an empirically derived Triple Debye model.⁵⁷ This approach is consistent with the model we previously presented.⁶⁰ To determine the maximum sensitivity of our system, various mixtures of ethanol and water are measured. As shown in Figs. 11(b)-11(d), one container is filled with pure water, while the second container is filled with various mixtures of water and ethanol. The ethanol proportion is varied non-linearly to assess the minimum step size that can be differentiated with steps from 50% to 2.5% by volume. In Fig. 11(e), the results of this measurement are presented. Container 1 contains water (green marks), while container 2 contains various ethanol-water mixtures (blue marks). These results are normalized to the maximum amplitude observed. We observe experimental results in line with Eq. (17) and a minimum differentiable step of 5%. With further calibration, we believe this result could be improved.

V. CONCLUSION

Here, we present an all-dielectric leaky-wave antenna for the terahertz range that can be monolithically integrated with a suite of other passive components composed entirely of high-resistivity, float-zone silicon. The antenna has an experimentally demonstrated operating bandwidth of 20%, in which the maximum gain is 19 dBi and a 3-dB frequency scanning field of view in excess of 34°. This antenna, coupled with a 3D printed COC lens, further enhances the in-plane gain by a further 6 dBi, reaching a maximum realized gain of 25 dBi. These components are mounted in a 3D printed package in order to realize a practical hand-held module. We apply this antenna module to the realization of a leaky wave radar by isolating individual angular components using the measured antenna radiation pattern, maximizing the angular and depth resolution

achievable with this antenna. With a range resolution in the order of 25 mm and an angular resolution above 10°, we can range and track optically hidden objects and differentiate between liquids incontainers. These techniques offer a feasible path toward real-time, single-shot imaging with integrated and mass fabricable terahertz technologies, which otherwise still remain elusive. Furthermore, the techniques presented here can be feasibly scaled to higher terahertz frequencies, where the performance of metallic antennas will be even further degraded, while the device design could be further optimized for increased depth or angular resolution depending on the application-specific requirements.

SUPPLEMENTARY MATERIAL

Obscured Object Tracking:

A video demonstrating real-time object tracking. A metallic optical post with a diameter of 12 mm is moved in front of the antenna module, while the position is tracked on the screen. Paper is introduced to obscure the post from view while the movement is repeated, showing that the position can still be retrieved.

In-Container Liquid Differentiation:

A video demonstrating the real-time differentiation of ethanol and water placed into high-density polyethylene containers. The first two empty containers are placed in front of the antenna module, then the left container is filled with ethanol, while the right container is filled with water. A distinctly stronger reflection is observed from the water filled container.

ACKNOWLEDGMENTS

The authors would like to thank Mr. Bryce Chung for his assistance with the 3D printing of the COC lens. This work was funded by the Australian Research Council (ARC) Grant No. DP220100489 and in part by CREST, JST (Grant No. JPMJCR21C4), KAKENHI, Japan (Grant No. 20H00249), and the commissioned research by NICT, Japan (03001). We acknowledge the assistance of Dr. Yoshiharu Yamada, Dr. Yusuke Kondo, and Dr. Hidemasa Yamane for their fabrication of the presented antenna. Daniel Headland acknowledges the support from the CONEX-Plus program funded by Universidad Carlos III de Madrid and the European Union's Horizon 2020 research and innovation program under the Marie Sklodowska–Curie Grant Agreement No. 801538.

AUTHOR DECLARATIONS

Conflict of Interest

The authors have no conflicts to disclose.

Author Contributions

Harrison Lees: Data curation (equal); Formal analysis (equal); Investigation (equal); Software (equal); Visualization (lead); Writing – original draft (lead); Writing – review & editing (equal). Daniel Headland: Conceptualization (equal); Formal analysis (equal); Methodology (equal); Software (equal); Supervision (equal);

Writing – original draft (supporting); Writing – review & editing (equal). Shuichi Murakami: Resources (equal); Writing – review & editing (supporting). Masayuki Fujita: Conceptualization (supporting); Funding acquisition (equal); Resources (equal); Supervision (supporting); Writing – review & editing (supporting). Withawat Withayachumnankul: Conceptualization (equal); Funding acquisition (equal); Project administration (lead); Resources (equal); Supervision (equal); Writing – original draft (supporting); Writing – review & editing (equal).

DATA AVAILABILITY

The data that support the findings of this study are available from the corresponding author upon reasonable request.

REFERENCES

- ¹R. Appleby and H. B. Wallace, "Standoff detection of weapons and contraband in the 100 GHz to 1 THz region," IEEE Trans. Antennas Propag. 55, 2944–2956 (2007).
- ²R. Cheville and D. Grischkowsky, "Time domain terahertz impulse ranging studies," Appl. Phys. Lett. **67**, 1960–1962 (1995).
- ³K. Iwaszczuk, H. Heiselberg, and P. U. Jepsen, "Terahertz radar cross section measurements," Opt. Express 18, 26399–26408 (2010).
- ⁴K. B. Cooper, R. J. Dengler, N. Llombart, T. Bryllert, G. Chattopadhyay, E. Schlecht, J. Gill, C. Lee, A. Skalare, I. Mehdi, and P. Siegel, "Penetrating 3-D imaging at 4- and 25-m range using a submillimeter-wave radar," IEEE Trans. Microwave Theory Tech. 56, 2771–2778 (2008).
- ⁵K. B. Cooper, R. J. Dengler, N. Llombart, B. Thomas, G. Chattopadhyay, and P. H. Siegel, "THz imaging radar for standoff personnel screening," IEEE Trans. Terahertz Sci. Technol. 1, 169–182 (2011).
- ⁶M. Hitzler, S. Saulig, L. Boehm, W. Mayer, W. Winkler, N. Uddin, and C. Waldschmidt, "Ultracompact 160-GHz FMCW radar MMIC with fully integrated offset synthesizer," IEEE Trans. Microwave Theory Tech. **65**, 1682–1691 (2017).
- ⁷K. Cooper, R. Dengler, N. Llombart, T. Bryllert, G. Chattopadhyay, I. Mehdi, and P. Siegel, "An approach for sub-second imaging of concealed objects using terahertz (THz) radar," J. Infrared, Millimeter, Terahertz Waves **30**, 1297–1307 (2009).
- ⁸K. Murata, K. Murano, I. Watanabe, A. Kasamatsu, T. Tanaka, and Y. Monnai, "See-through detection and 3D reconstruction using terahertz leaky-wave radar based on sparse signal processing," J. Infrared, Millimeter, Terahertz Waves 39, 210–221 (2018).
- ⁹H. Matsumoto, I. Watanabe, A. Kasamatsu, and Y. Monnai, "Integrated terahertz radar based on leaky-wave coherence tomography," Nat. Electron. 3, 122–129 (2020).
- ¹⁰Y. Ito and Y. Monnai, "Dynamic phase measurement for vibrometry based on leaky-wave terahertz radar," in *2021 IEEE Asia-Pacific Microwave Conference (APMC)* (IEEE, 2021), pp. 339–340.
- ¹¹ M. Fujita and T. Nagatsuma, "Photonic crystal technology for terahertz system integration," Proc. SPIE **9856**, 98560P (2016).
- ¹² A. Suminokura, T. Ishigaki, M. Fujita, and T. Nagatsuma, "Grating coupler for terahertz-wave integrated circuits," in *Asia-Pacific Radio Science Conference (AP-RASC)* (URSI, 2013), Vol. 9856, p. DJ2b-3.
- ¹³ H. Zhang, C. Liang, J. Song, C. Fu, X. Zang, L. Chen, and J. Xie, "Terahertz out-of-plane coupler based on compact spot-size converter," Chin. Opt. Lett. 20, 021301 (2022).
- ¹⁴D. Jahn, M. Weidenbach, J. Lehr, L. Becker, F. Beltrán-Mejía, S. F. Busch, J. C. Balzer, and M. Koch, "3D printed terahertz focusing grating couplers," J. Infrared, Millimeter, Terahertz Waves 38, 708–716 (2017).
- ¹⁵H. Guerboukha, M. Sakaki, R. Shrestha, J. Li, N. Benson, and D. M. Mittleman, "Photonic crystal THz leaky-wave antenna 3D-printed in alumina," in 2023 48th International Conference on Infrared, Millimeter, and Terahertz Waves (IRMMW-THz) (IEEE, 2023).

- ¹⁶K. Murano, S. Fukuma, S. Suzuki, M. Asada, W. Withayachumnankul, T. Tanaka, and Y. Monnai, "Design of terahertz leaky-wave antenna driven by resonant-tunneling diode," in 2017 42nd International Conference on Infrared, Millimeter, and Terahertz Waves (IRMMW-THz) (IEEE, 2017).
- ¹⁷N. J. Karl, R. W. McKinney, Y. Monnai, R. Mendis, and D. M. Mittleman, "Frequency-division multiplexing in the terahertz range using a leaky-wave antenna," Nat. Photonics **9**, 717–720 (2015).
- ¹⁸ H. Guerboukha, R. Shrestha, J. Neronha, O. Ryan, M. Hornbuckle, Z. Fang, and D. Mittleman, "Efficient leaky-wave antennas at terahertz frequencies generating highly directional beams," Appl. Phys. Lett. 117, 261103 (2020).
- ¹⁹Q. L. Zhang, B. J. Chen, K. F. Chan, and C. H. Chan, "Terahertz circularly-and linearly polarized leaky-wave antennas based on spin-orbit interaction of spoof surface plasmon polaritons," IEEE Trans. Antennas Propag. 69, 4347–4358 (2021).
- ²⁰M. Steeg, N. Yonemoto, J. Tebart, and A. Stöhr, "Substrate-integrated waveguide PCB leaky-wave antenna design providing multiple steerable beams in the V-band," Electronics 6, 107 (2017).
- ²¹ P. Lu, T. Haddad, B. Sievert, B. Khani, S. Makhlouf, S. Dülme, J. F. Estévez, A. Rennings, D. Erni, U. Pfeiffer, and A. Stohr, "InP-based THz beam steering leaky-wave antenna," IEEE Trans. Terahertz Sci. Technol. 11, 218–230 (2021).
- ²²P. Lu, T. Haddad, J. Tebart, M. Steeg, B. Sievert, J. Lackmann, A. Rennings, and A. Stöhr, "Mobile THz communications using photonic assisted beam steering leaky-wave antennas," Opt. Express 29, 21629–21638 (2021).
- ²³ D. Headland, M. Fujita, and T. Nagatsuma, "Bragg-mirror suppression for enhanced bandwidth in terahertz photonic crystal waveguides," IEEE J. Sel. Top. Quantum Electron. 26, 1 (2020).
- ²⁴W. Gao, W. S. L. Lee, X. Yu, M. Fujita, T. Nagatsuma, C. Fumeaux, and W. Withayachumnankul, "Characteristics of effective-medium-clad dielectric waveguides," IEEE Trans. Terahertz Sci. Technol. 11, 28–41 (2021).
- ²⁵D. Headland, M. Fujita, G. Carpintero, T. Nagatsuma, and W. Withayachumnankul, "Terahertz integration platforms using substrateless all-silicon microstructures," APL Photonics **8**, 091101 (2023).
- ²⁶W. Gao, W. S. Lee, C. Fumeaux, and W. Withayachumnankul, "Effective-medium-clad Bragg grating filters," APL Photonics **6**, 076105 (2021).
- ²⁷P. Dechwechprasit, C. Fumeaux, and W. Withayachumnankul, "Integrated disk resonator on substrateless dielectric waveguide platform for terahertz switch applications," in 2022 47th International Conference on Infrared, Millimeter And Terahertz Waves (IRMMW-THz) (IEEE, 2022).
- ²⁸W. Withayachumnankul, R. Yamada, M. Fujita, and T. Nagatsuma, "All-dielectric rod antenna array for terahertz communications," APL Photonics 3.051707 (2018)
- ²⁹D. Headland, W. Withayachumnankul, R. Yamada, M. Fujita, and T. Nagatsuma, "Terahertz multi-beam antenna using photonic crystal waveguide and Luneburg lens," APL Photonics 3, 126105 (2018).
- ³⁰J. Liang, W. Gao, H. Lees, and W. Withayachumnankul, "All-silicon terahertz planar horn antenna," IEEE Antennas Wireless Propag. Lett. **20**, 2181–2185 (2021).
- ³¹X. Yu, J.-Y. Kim, M. Fujita, and T. Nagatsuma, "Efficient mode converter to deep-subwavelength region with photonic-crystal waveguide platform for terahertz applications," Opt. Express 27, 28707–28721 (2019).
- ³²D. J. Headland, Y. Nishida, X. Yu, M. Fujita, and T. Nagatsuma, "Terahertz oscillator chips backside-coupled to unclad microphotonics," IEEE J. Sel. Top. Quantum Electron. 29, 1 (2023).
- ³³D. Headland, W. Withayachumnankul, M. Fujita, and T. Nagatsuma, "Gratingless integrated tunneling multiplexer for terahertz waves," Optica 8, 621–629 (2021).
- ³⁴D. Headland and W. Withayachumnankul, "Continuous leakage from slow-wave structure for integrated all-dielectric uniform leaky wave antenna," in 2022 16th European Conference on Antennas and Propagation (EuCAP) (IEEE, 2022).
- ³⁵S. Kim, D. A. Westly, B. J. Roxworthy, Q. Li, A. Yulaev, K. Srinivasan, and V. A. Aksyuk, "Photonic waveguide to free-space Gaussian beam extreme mode converter," Light: Sci. Appl. 7, 72 (2018).
- ³⁶D. Zheng, G.-B. Wu, D. Wang, K. F. Chan, K. Wu, and C. H. Chan, "Planar leaky-wave antenna featuring wideband fixed-beam radiation and tailorable directional angle for millimeter-wave applications," IEEE Trans. Antennas Propag. 71, 3238–3250 (2023).

- ³⁷D. R. Jackson, C. Caloz, and T. Itoh, "Leaky-wave antennas," Proc. IEEE 100,
- 38D. Headland and W. Withayachumnankul, "Leaky-mode analysis of microstructured dielectric waveguides toward integrated tunneling multiplexers with enhanced bandwidth," in 2021 IEEE Asia-Pacific Microwave Conference (APMC) (IEEE, 2021), pp. 335-337.
- ³⁹ J. Dai, J. Zhang, W. Zhang, and D. Grischkowsky, "Terahertz time-domain spectroscopy characterization of the far-infrared absorption and index of refraction of high-resistivity, float-zone silicon," J. Opt. Soc. Am. B 21, 1379-1386 (2004).
- ⁴⁰S. J. Jang, Y. M. Song, C. I. Yeo, C. Y. Park, J. S. Yu, and Y. T. Lee, "Antireflective property of thin film a-Si solar cell structures with graded refractive index structure," Opt. Express 19, A108–A117 (2011).

 41 W. H. Southwell, "Gradient-index antireflection coatings," Opt. Lett. 8, 584–586
- (1983).
- ⁴²J. K. Kim, A. N. Noemaun, F. W. Mont, D. Meyaard, E. F. Schubert, D. J. Poxson, H. Kim, C. Sone, and Y. Park, "Elimination of total internal reflection in GaInN light-emitting diodes by graded-refractive-index micropillars," Appl. Phys. Lett. 93, 221111 (2008).
- ⁴³T. C. Choy, Effective Medium Theory: Principles and Applications (Oxford University Press, 2015), Vol. 165.
- 44B. E. Saleh and M. C. Teich, Fundamentals of Photonics (John Wiley & Sons, 2019).
- ⁴⁵D. Headland, X. Yu, M. Nagai, M. Fujita, and T. Nagatsuma, "Packaged dish antenna for wireless terahertz photonic crystal waveguide devices," in 2020 International Symposium on Antennas and Propagation (ISAP) (IEEE, 2021)
- ⁴⁶S. F. Busch, M. Weidenbach, J. C. Balzer, and M. Koch, "THz optics 3D printed with TOPAS," J. Infrared, Millimeter, Terahertz Waves 37, 303-307 (2016).
- ⁴⁷B. Chung, H. Lees, D. Headland, and W. Withayachumnakul, "Broadband and efficient terahertz beam scanning using a 3D-printed risley prism," in 2022 47thInternational Conference on Infrared, Millimeter and Terahertz Waves (IRMMW-THz) (IEEE, 2022).
- ⁴⁸A. Sengupta, A. Bandyopadhyay, B. Bowden, J. Harrington, and J. Federici, "Characterisation of olefin copolymers using terahertz spectroscopy," Electron.
- ⁴⁹D. Zwyssig, E. Hack, P. Zolliker, and E. Mavrona, "3D printed microfluidic devices using TOPAS filament for THz spectroscopic measurements," Opt. Mater. Express 13, 1031-1040 (2023).

- ⁵⁰E. Mavrona, J. Graf, E. Hack, and P. Zolliker, "Optimized 3D printing of THz waveguides with cyclic olefin copolymer," Opt. Mater. Express 11, 2495-2504
- ⁵¹Y. Alvarez, R. Camblor, C. Garcia, J. Laviada, C. Vazquez, S. Ver-Hoeye, G. Hotopan, M. Fernandez, A. Hadarig, A. Arboleya, and F. Las-Heras, "Submillimeter-wave frequency scanning system for imaging applications," IEEE Trans. Antennas Propag. 61, 5689-5696 (2013).
- $^{\bf 52}{\rm Y}.$ Ito and Y. Monnai, "Unambiguous detection of multiple objects using leakywave terahertz radar based on stepwise signal processing," in 2020 45th International Conference on Infrared, Millimeter, and Terahertz Waves (IRMMW-THz)
- ⁵³A. F. Fercher, W. Drexler, C. K. Hitzenberger, and T. Lasser, "Optical coherence tomography - principles and applications," Rep. Prog. Phys. 66, 239
- 54K. Murano, I. Watanabe, A. Kasamatsu, S. Suzuki, M. Asada, W. Withayachumnankul, T. Tanaka, and Y. Monnai, "Low-profile terahertz radar based on broadband leaky-wave beam steering," IEEE Trans. Terahertz Sci. Technol. 7,
- ⁵⁵S. Iwamatsu, M. Ali, J. L. Fernández-Estévez, J. Tebart, A. Kumar, S. Makhlouf, G. Carpintero, and A. Stöhr, "Ultra-wideband multi-octave planar interconnect for multi-band THz communications," J. Infrared, Millimeter, Terahertz Waves 44, 532, (2023).
- ⁵⁶L. Thrane, R. H. Jacobsen, P. Uhd Jepsen, and S. Keiding, "THz reflection spectroscopy of liquid water," Chem. Phys. Lett. 240, 330-333 (1995).
- ⁵⁷P. U. Jepsen, U. Møller, and H. Merbold, "Investigation of aqueous alcohol and sugar solutions with reflection terahertz time-domain spectroscopy," Opt. Express **15**, 14717–14737 (2007).
- ⁵⁸P. U. Jepsen, J. K. Jensen, and U. Møller, "Characterization of aqueous alcohol solutions in bottles with THz reflection spectroscopy," Opt. Express 16, 9318-9331 (2008).
- 59 S. Busch, M. Weidenbach, M. Fey, F. Schäfer, T. Probst, and M. Koch, "Optical properties of 3D printable plastics in the THz regime and their application for 3D printed THz optics," J. Infrared, Millimeter, Terahertz Waves 35, 993-997
- ⁶⁰H. Lees, C. Hayes, and W. Withayachumnankul, "Terahertz coherence tomography for in-container liquid characterization," IEEE J. Sel. Top. Quantum Electron. 29, 8600408 (2023).